Phase-field-simulation of the static recrystallization and grain growth kinetics of ultrafine-grained aluminum processed by high pressure torsion extrusion

Olena Abramova [a,*], Dayan Nugmanov [a], Daniel Schneider [a,c], Andreas Prahs [b], Tobias Mittnacht [b], Julia Ivanisenko [a], Brigitte Baretzky [a], Britta Nestler [a,b,c]

[a] Institute of Nanotechnology (INT), Karlsruhe Institute of Technology, 76131, Karlsruhe, Germany
[b] Institute of Applied Materials (IAM), Karlsruhe Institute of Technology, 76131, Karlsruhe, Germany
[c] Institute of Digital Materials Science, Karlsruhe University of Applied Sciences, 76133, Karlsruhe, Germany

Keywords:
Recrystallization
Grain growth simulation
Phase-field model

A B S T R A C T

The kinetics of recrystallization of ultrafine-grained aluminum during post-deformation annealing at 300°C are presented. A multiphase-field model was applied to generate a digital twin of the recrystallization kinetics in pure Al subjected to severe plastic deformation by high-pressure torsional extrusion. The experimental map of dislocation orientation and density distribution was directly imported into the Pace3D software package to simulate the recrystallization process. Using the digital twin, we were able to account for the change in driving force during recrystallization and simulate the kinetics of normal grain growth observed experimentally up to 60 min of annealing. It was demonstrated that the kinetics of grain growth in the region of short-term annealings exhibits a sigmoidal character, which could not be verified experimentally for extremely short annealings, lasting less than one minute.

1. Introduction

Despite many years of studying recrystallization (ReX) kinetics, this problem remains a subject of research in materials undergoing severe plastic deformation (SPD). Control of ReX kinetics is a way to stabilize the morphology undergoing grain refinement and improve the performance and technological properties of ultrafine-grained (UFG) materials, which occur as a result of recovery and ReX. In particular, ReX kinetics of materials deformed to large strains can develop via discontinuous (DRex) and continuous recrystallization (CReX) mechanisms [1,2]. CReX operates without the nucleation stage via migration of high-angle grain boundaries (HAGB) and change in boundary misorientation angles. The misorientation angle of a grain boundary can increase [3] or decrease [4], depending on the annealing temperature. Finally, small-scale boundary migration provides normal grain growth. Comprehending the principles underlying ReX necessitates the identification of governing parameters that induce and restrain coarsening through the regulation of grain boundary migration. Small-scale grain boundary migration provides normal grain growth, which is described by an Arrhenius-type equation [5]:

$$D^2 - D_0^2 = 2\alpha\gamma M \cdot t = kt, \tag{1}$$

with D as the mean grain diameter, the initial mean grain diameter D_0 at time $t = 0$ and a geometric constant α. The interfacial energy γ, and the grain boundary mobility M are assumed to be uniformly and constant for all grain boundaries. The introduced parameter $k = 2\alpha\gamma M$ is used to quantify the evolution of the mean grain size.

Experiment with static recrystallization. ReX kinetics are strongly dependent on the stacking fault energy [6]. For aluminum, a material with high stacking fault energy, the mechanism of CReX operates over a wide range of annealing temperatures. There are reports that in Al 1050 and Al-0.4Zr deformed by high-pressure torsion, short-term annealing at intermediate temperatures of 150–230 °C leads to Arrhenius-type grain growth and additional hardening [7,8]. The characteristic features of recrystallization structures of aluminum under these annealing conditions are indicative of the development of CReX with normal grain growth.

In general, models describing grain growth in polycrystalline microstructures suggest that excess interfacial energy, which is equivalent to grain boundary energy in this context, acts as a driving force for boundary migration. This excess energy serves as the primary mechanism promoting boundary movement and, consequently, grain

* Corresponding author.
E-mail address: olena.abramova@kit.edu (O. Abramova).

growth [9–11]. Assuming equal or nearly equal interfacial energy for all grain boundaries, the mean grain diameter increases correspondingly at low temperatures according to Eq. (1), a phenomenon confirmed by both theory [11,12] and computer simulations [13–15].

As captured by Eq. (1), grain boundary mobility is a controlling factor determining the microstructure after recrystallization. For annealed aluminum at temperatures below 400 K, Winning et al. [16] demonstrated experimentally that the mobility M for low-angle grain boundaries (LAGBs) is lower than that of HAGBs. Conversely, a higher annealing temperature of 900 K provides a higher mobility of grains, which can result in various recrystallization mechanisms at different temperatures [8]. This finding is in good agreement with the experimental observation that the LAGB network exhibits higher stability than the HAGB network during annealing after deformation at temperatures below 573 K, both after conventional deformation [17,18] and after SPD by accumulated roll bonding [4], equal channel angular extrusion [19], and high-pressure torsion extrusion (HPTE) [20]. In cases where the formation of recrystallization nuclei is not required due to the presence of ultrafine grains with predominantly HAGB, it becomes important to consider the migration kinetics of existing LAGBs and HAGBs, as well as the change in misorientation angles of these boundaries during annealing.

The recrystallization process was developed in the three-dimensional structure of the aluminum to avoid the effects of the surface and surface oxidation on grain boundary (GB) motion.

Simulation of the static recrystallization. In order to compare the kinetics of ReX at the same temperature in aluminum subjected to different kinds of deformation, it is important to consider a significant difference in the initial grain size, dislocation density, texture, i.e. parameters that determine the development of ReX. The prediction of the microstructure evolution during annealing poses a complex problem regarding the influence of the microstructure features on the ReX kinetics. In particular, the stored energy of deformation in majority of physical models of ReX is considered as an integral parameter. In general, most modeling methods assume that the process of recrystallization (ReX) evolves via the formation and growth of nuclei [21]. Since the recrystallization processes in severely deformed materials with high stacking fault energy are not well understood, we designed a digital twin to simulate the annealing of the aluminum microstructure, taking into account static recrystallization processes using the multiphase-field method (MPFM). The MPFM is expected to provide new insights into the changes in recrystallization and grain growth kinetics during the annealing of an aluminum polycrystalline material.

Conventional models of ReX such as classical theory of heterogeneous nucleation growth [21,22] considered the development of ReX through the formation and growth of nuclei. However, these models do not take into account the experimentally obtained GND density as the basis for the bulk free energy. In the case of modeling ReX using the MPFM, the current speed of movement of the boundaries is determined by the ratio of energy potentials. The magnitude of the potentials of neighboring grains determines the kinetics of boundary motion. Therefore, the nucleation process does not need to be addressed by the approach used in this work, which creates a digital twin of the ReX process used to simulate the complex competitive process of grain growth. Creating a digital twin of the real structure formed during ReX make it possible to operate with big data with the calculation of the mutual influence of structural factors.

The PACE3D software package [23], based on MPFM, facilitates the expression of new details in the study of the ReX kinetics of aluminum polycrystalline material. Since ReX processes developing in highly deformed high stacking fault energy materials are still subject of current research, we used MPFM to simulate ReX and developed a digital twin of the aluminum microstructure after recovery and static ReX.

Objective and originality of the current work. In order to reproduce the ReX process, it is necessary to utilize the actual measured distribution of dislocation density in the structure in order to formulate the driving force. The primary objective of this investigation is to characterize the recrystallization process in UFG aluminum during annealing at 300 °C, both by simulations and experiments.

Considering the complexity of the subject under investigation and the variety of processes occurring during recrystallization, this work focuses on the driving forces that facilitate the movement of boundaries. These driving forces aim to minimize the free energy accumulated during previous deformation and reduce the interfacial energy. The driving force in our study specifically depends on the actually measured dislocation density, which is a novel aspect compared to previous works that considered nucleation criteria based only on the GND-density.

Unlike other studies, this work compares MPFM simulations directly to experimental results, demonstrating a good agreement between the simulated and experimental data. This integrated approach enhances the understanding of recrystallization kinetics in UFG aluminum, providing new insights into the changes in recrystallization and grain growth during annealing.

2. Experimental methods

2.1. Used material and specimens

Material. Commercially pure aluminum rod samples containing 99.5 Al, 0.3–0.4 Si, less than 0.1–0.2 Fe, Mg, Co and other impurities (all wt.%, AA1050, supplied by MaTeck Material Technologie & Kristalle GmbH) were machined, extruded from 20.0 to 11.8 mm diameter and annealed at 345 °C for 30 min, with final water cooling to room temperature. The thermal treatment was performed to reduce residual stresses and achieve a homogeneous microstructure. Cylindrical aluminum samples with a length of 35 mm were processed at room temperature using a computer-controlled HPTE machine (manufacturer: W. Klement GmbH, Lang, Austria). Molybdenum disulfide (MoS_2) was used as a lubricant in all experiments to facilitate the extrusion process. The HPTE equipment used in this study has been described in detail in [24], using an advanced hexagonal shape of HPTE dies [25].

Processing of the as-deformed samples and experiment on the annealing. The samples were individually extruded through the die, using a punch moving at an extrusion speed v and a lower die rotating at a rotational speed ω. As a result, the specimens underwent both expansion–extrusion deformation and torsional deformation in a narrow zone where both dies meet. The billets were annealed at 300 °C and subsequently quenched in water. The duration of the annealing process was varied from 10 to 60 min. The scheme of deformation and subsequent annealing is shown in Fig. 1a. Each as-deformed sample was annealed with different annealing times and quenched in water to fix the microstructure of the state. After annealing, the samples were sectioned with a metallography saw equipped by the water cooling for the next microstructural characterization of the section plane.

2.2. Image generation and processing

Generation of EBSD images. Microstructure investigations were performed using a scanning electron microscope: Zeiss LEO and Zeiss Auriga 60 (SEM), operating at 20 kV. The Zeiss Auriga 60 scanning electron microscope with electron backscatter diffraction (EBSD) detector was used to analyze grain morphology and grain boundary misorientations. To prepare the samples for analysis, they were initially sectioned perpendicular to the extrusion axis, then grinded and mechanically polished. Finally, at room temperature, discs with a diameter of 3 mm and a thickness of ~150 μm were electropolished using the A3 electrolyte by Struers. Electropolishing was performed at a voltage of 20 V and a current of 10 A.

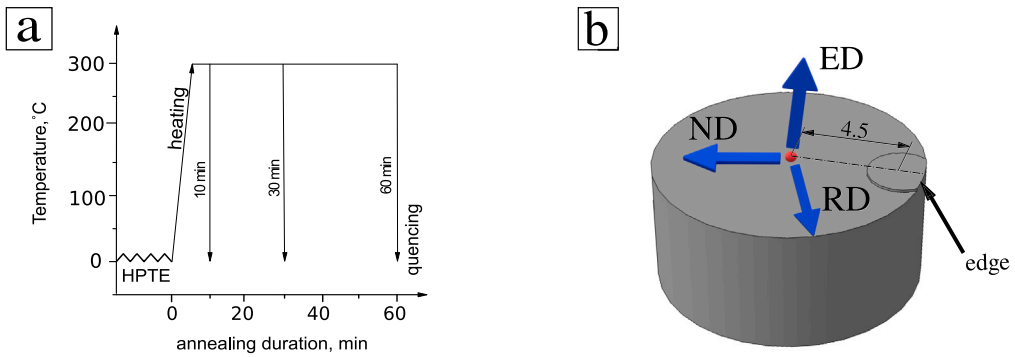

Fig. 1. Schematic representation of the annealing (a) and the external directions at the location of the normal section of the billet selected for EBSD analysis (b).

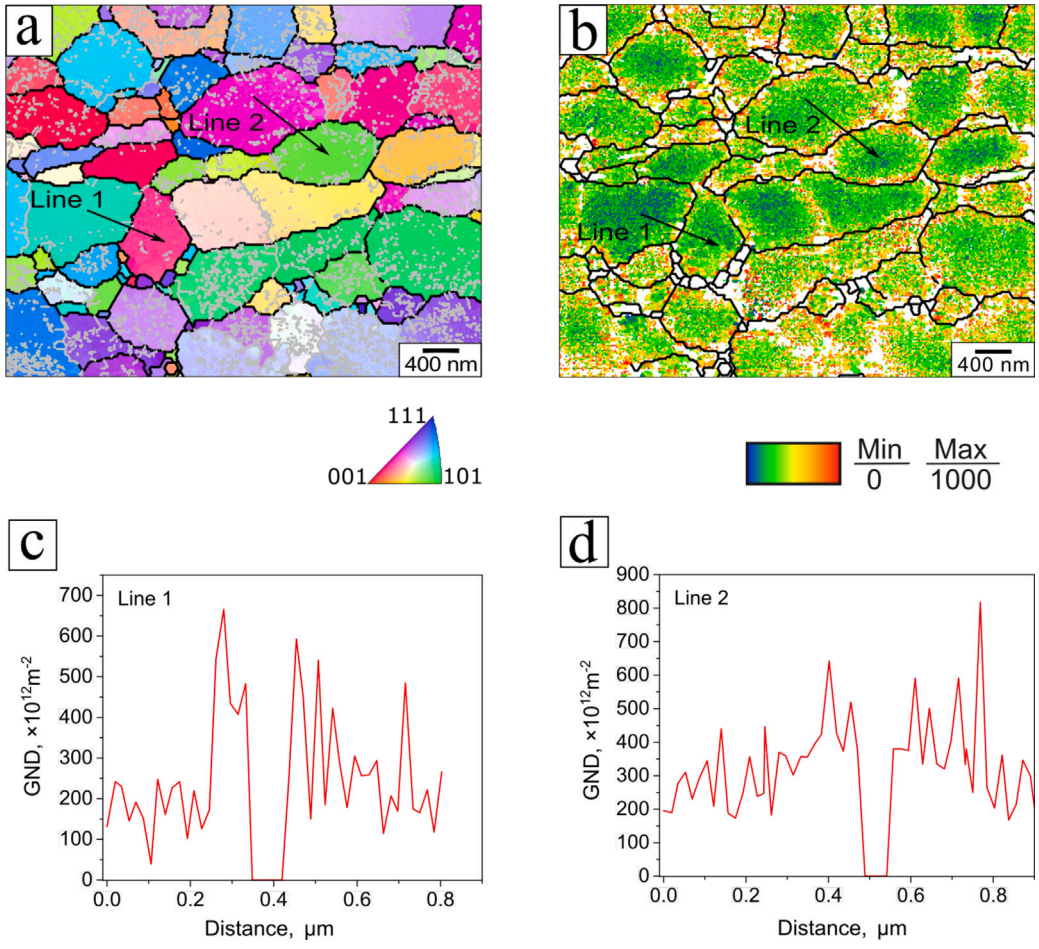

Fig. 2. Experimentally obtained microstructure of the HPTE-processed Al before annealing. Inverse pole figure map (a) shows a typical area of aluminum structure. Geometrically necessary dislocation density distribution (b) is shown in a color-coded map at the scale [$\times 10^{12}$ m^{-2}]. The outer directions, the standard stereographic triangle, and the GND density scale are shown in the lower part of the figure. HAGBs are indicated by the black lines, LAGBs — by the gray lines. GND distributions along the lines 1 and 2 are represented in (c) and (d) accordingly. GND are scaled to [$\times 10^{12}$ m^{-2}] in the graphs (c, d).

Processing of EBSD images. The microstructure evolution of HPTE treated specimens was investigated at the transverse cross-section located at the middle of the billet height during annealing. The EBSD images were evaluated using the orientation imaging microscopy (OIM) software by EDAX. The scanning step size ranged from 25 nm to 1 μm, which corresponds to the size of one pixel. The EBSD study was performed on the transverse section of the HPTE-processed specimens near the edge, specifically at approximately ~4.0 mm from the central axis of the rod. The edge region was selected as the focus of the investigation due to the gradient nature of the strain distribution during HPTE processing and the resulting maximal grain refinement at the edge of the rod cross-section. The horizontal direction of the rectangular scan plane was parallel to the outer radial direction, and the vertical direction was parallel to the normal direction (see Fig. 1b). The minimum percentage indexation of the OIM maps was obtained in the HPTE-processed state and was 81 %. The states resulting from annealing are distinguished by coarse grain size and higher percent indexation, reaching 93 % after annealing for 60 min. In order to guarantee the dependability of the

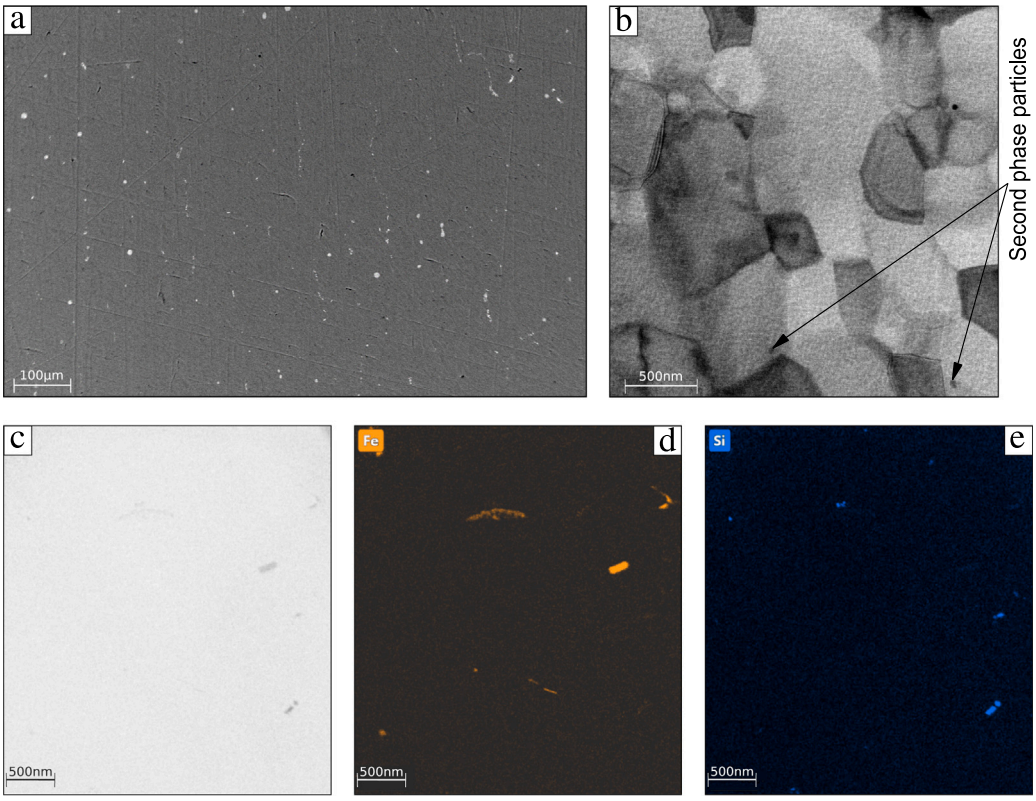

Fig. 3. SEM EBSD (a), dark-field — transmission electron microscopy (b) and high-angle annular dark-field scanning transmission electron microscopy (c) images of UFG pure aluminum of the as-deformed state. Energy dispersive X-ray spectroscopy mapping of elements Fe (d), and Si (e).

EBSD data, a cleaning procedure was implemented utilizing the grain dilation cleanup and neighbor orientation correlation options of the OIM software. With regard to the neighbor orientation correlation, the 5th neighbors criterion and a maximum coefficient indexation (CI) factor of 0.2 were employed.

To analyze the microstructure, the grain size and grain boundary misorientations were characterized. Grains consisting of four pixels or less were automatically included in neighboring grains. The grain tolerance angle for the dilation cleanup process was set at 15°. Additionally, a lower limit boundary misorientation threshold of 2° was applied to eliminate potentially disputable orientations resulting from orientation noise.

To distinguish between LAGBs and HAGBs, a threshold value of 15° was considered [26]. The volume fraction of HAGBs (V_{HAGBs}) was determined as the fraction of misorientations larger than 15° in the total set of misorientations.

Grain size was calculated using the equal diameter method [27]. Accordingly, the mean diameter of a circle whose surface area is equal to the surface area of a crystallite bounded by boundaries with misorientations of 15° and higher is named grain size (D). Histograms of the grain size distributions were plotted for specific area fractions (s_i/S) of the corresponding crystallite size intervals.

The characterization of grain elongation was determined by calculating the ratio of the number of intersections of lines drawn along the normal direction and radial direction with grain boundaries, represented by N_{ND} and N_{RD}, respectively.

The minimal resolution of the SEM EBSD detector is not exceed 0.5° regarding the used voltage of 20 kV. However, it is enough to resolve all low-angle boundaries (with misorientations $2° < \theta < 15°$) and high-angle boundaries ($\theta > 15°$) [26,28]. The critical angle of 2° was considered the lowest measurable value of subgrain and grain boundaries misorientation. Misorientations smaller than 2° were considered integral misorientations, which occur as a consequence of the local curvature of the crystal lattice due to geometrically necessary dislocations (GND).

The GND density values were calculated using TSL OIM EDAX v.7 software (EDAX Inc., Draper, UT, USA). The software employed default settings for face-centered cubic (fcc) crystal-type slip systems. The calculation of GND density specifically considered slip in (111) crystallographic planes and three close-packed ⟨110⟩ directions for each of the ⟨111⟩ slip plane. The GND density was determined using the GND map reconstruction option. Additional information regarding the GND density calculation can be found in a separate Ref. [29].

3. Experimental results

3.1. Orientation imaging, mean grain size and grain boundary misorientations

Characterization of the initial state. High-resolution OIM map (scan step is 20 nm) of the HPTE-processed aluminum is shown in Fig. 2. It is well-established that the UFG structure formed after SPD contains a significant number of LAGBs. As a result, almost all grains are bounded by both high- and LAGBs. This can also be observed in the structure of HPTE-processed aluminum (Fig. 2a). Since the mobility of LAGBs is much lower than the mobility of HAGB, the analysis of the kinetics of recrystallization and grain growth in such materials has a number of peculiarities.

Reconstructed inverse pole images (Fig. 2a) and the maps of the GND distribution (Fig. 2b) are considered for the purpose of comparing the simulations and experimental results in terms of statistically determined quantitative characteristics. In the deformed state (Fig. 2a), the aluminum specimen exhibits slightly elongated grains with an aspect ratio $N_{ND}/N_{RD} = 1.23$, a normal grain size distribution, and average grain size of $D = 1.3\,\mu m$ (Fig. 2a). The GND distribution in the initial state demonstrates the gradual increase of the GND value from the center of the grain to its boundary (Fig. 2c, d).

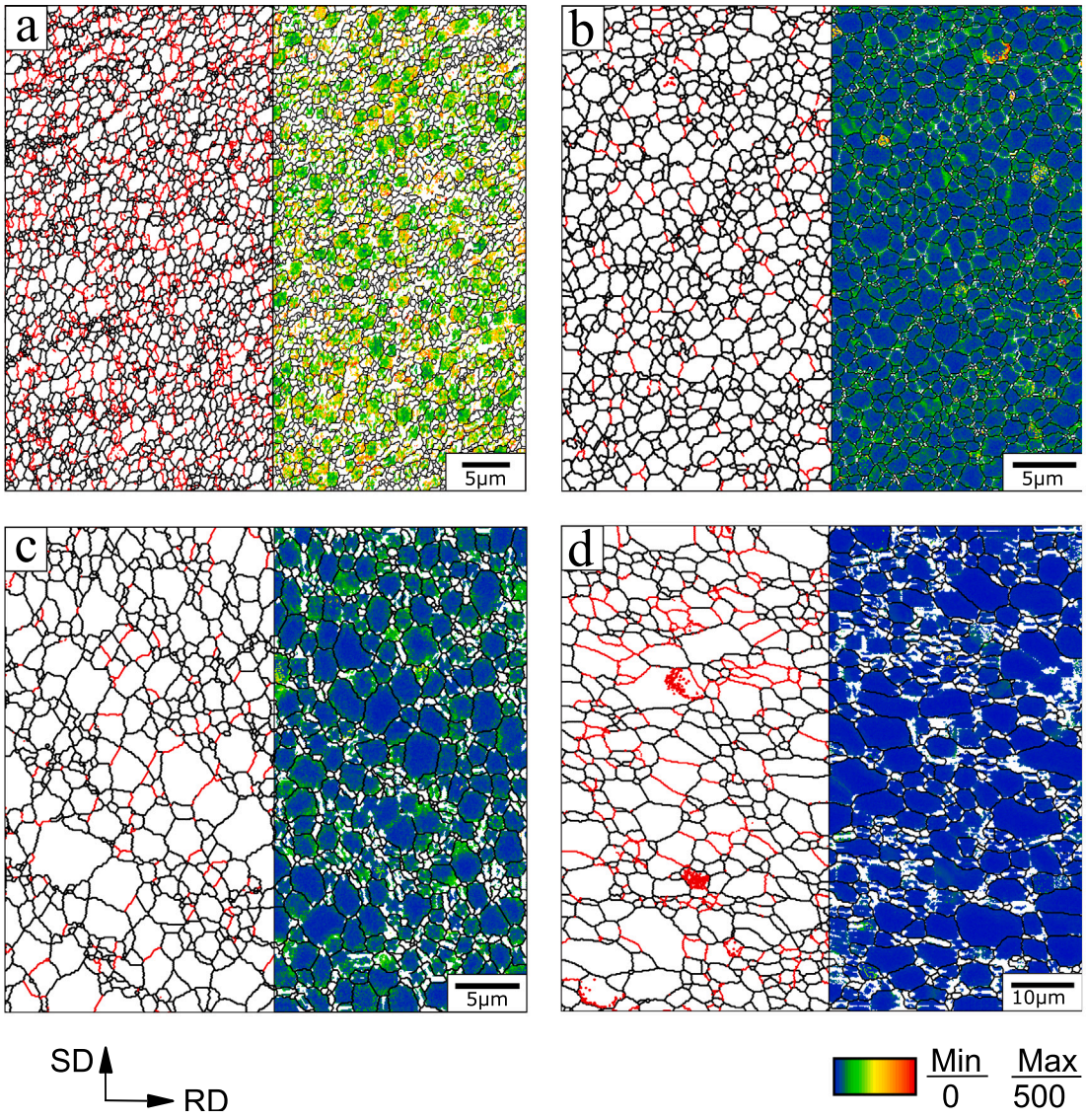

Fig. 4. Microstructure of the HPTE-processed Al in the deformed state (a) and after annealing at 300°C for 10 min (b), 30 min (c), and 60 min (d). Grain boundary networks (left images) show typical microstructures. Geometrically necessary dislocation density distributions (right images) are shown in a color-coded map at the scale [$\times 10^{12} m^{-2}$]. The deformation directions and the GND density scale are shown in the lower part of the figure. HAGBs are indicated by the black lines LAGBs by red lines.

Fig. 3a presents the scanning electron microscopy (a), transmission electron microscopy dark field (b), high-angle annular dark-field scanning transmission electron microscopy images (c), and energy dispersive X-ray spectroscopy mapping (d, e) of UFG pure aluminum.

The amount of Si and Fe content in the Al matrix is 0.41 ± 0.02 wt.%, according to SEM energy dispersive X-ray spectroscopy analysis. The remainder of the Si is accumulated in coarse particles. TEM elemental analysis maps by electron energy loss spectroscopy indicate the excess near-spherical particles with a length of 200–500 nm containing Fe and Si (Fig. 3a, d, e). The coarse particles are metallurgical impurities in the Al–Si–Fe system. Additionally, second phase particles with a globular morphology were present within the subgrain/grains and at the GBs. Energy dispersive X-ray spectroscopy mapping showed that these particles were AlFe and AlFeSi phases, with an average size of ~240 nm (Fig. 3d, e). Such dispersed fine particles may have a pinning effect on the GB motion, which hinders the recrystallization process.

Characterization of the microstructure evolution after annealing at 300 ° C. The grain boundary networks of the microstructure of HPTE-processed aluminum before (a) and after annealing (b–d) are shown in Fig. 4. The microstructure evolution of UFG annealed samples was quantitatively characterized by EBSD. The initial structure shown in Fig. 4a is used as the input for the ReX simulation studies. Quantitative analysis of EBSD maps indicates that with the increase of annealing time, the initial UFG structure changed significantly due to recrystallization. Annealing for 10 and 30 min results in grain growth and formation of equiaxed grains, indicated by a decreased N_{ND}/N_{RD} ratio as presented in Table 1.

After annealing for 60 min and resulted in an incremental increase in grain size D, as shown in Fig. 4b, c. An important feature of the structure after annealings for 30 and 60 min is the presence of large grains with low GND density (grains with a size of $D = 10\,\mu m$ or more in Fig. 4b, c). In contrast, small grains of 1–2 μm in size contain high GND density. After 60 min of annealing (Fig. 4d), the average GND density is rather low, and apparently, there is no correlation between grain size and GND density. It is important to note that in the initial state, a majority of the grain boundaries were curved, which is considered evidence of the non-equilibrium state of boundaries

Table 1
Microstructure parameters obtained from OIM: the grain size D, the volume fraction of HAGBs (V_{HAGBs}), the average misorientation angle of the full map Θ, the ratio N_{ND}/N_{RD}, and density of GNDs.

Process ID	D (μm)	V_{HAGBs} (%)	Θ (°)	N_{ND}/N_{RD}	GND ($\times 10^{12}$ m^{-2})
as-deformed	1.3	78.4	32.8	1.23	172.5
10 min	1.6	90.1	37.8	1.08	115.9
30 min	2.3–6.0	91.5	38.0	0.88	38.1
60 min	6.7–27.3	72.4	32.9	0.79	21.7

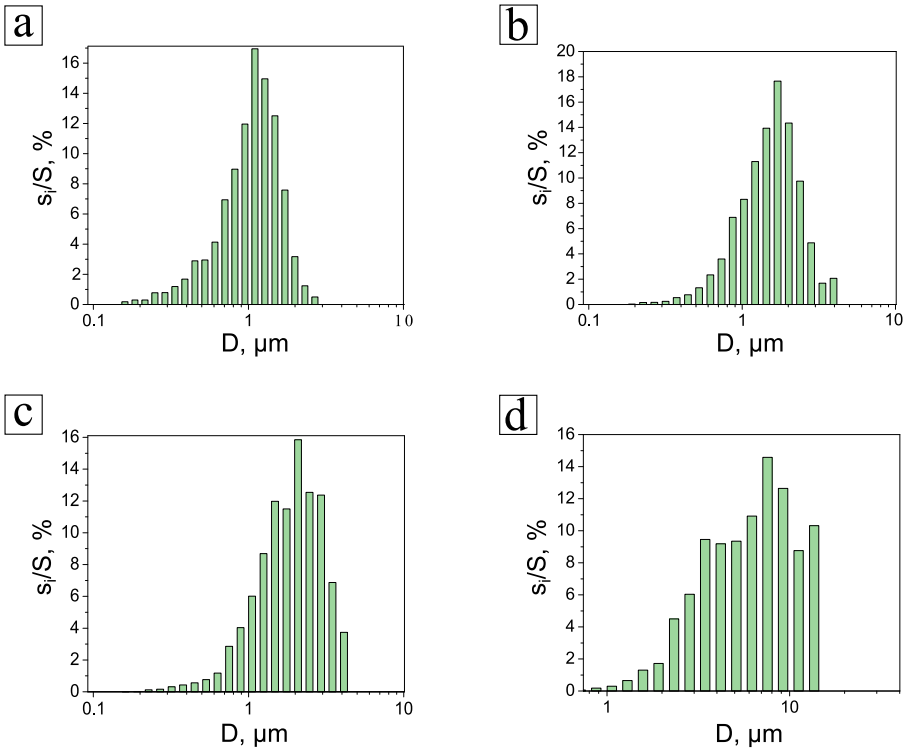

Fig. 5. Grain size distribution with respect to the specific area (s_i/S) in the microstructure of HPTE-processed Al: (a) in the deformed state and after annealing at 300 °C for (b) 10 min, (c) 30 min, and (d) 60 min.

according to Ref. [30]. The curved shape can be observed after 10, 30, and 60 min of annealing, as shown in Fig. 4b–d.

3.2. Geometrically necessary dislocations

Effect of annealing on GND density ρ_d. In Fig. 4, the images on the right show the distributions of GND density values of the same areas shown in the grain boundaries networks on the left. In the initially deformed structure, the GND density has a minimum value in the center of the grain and increases towards the grain boundary (Fig. 4a). Annealing for 30 min resulted in a sharp decrease in the average GND density from 172×10^{12} m^{-2} in the deformed state to 38.1×10^{12} m^{-2} (Table 1). A further decrease of the GND density can be observed after 30 and 60 min of annealing (Table 1). The most important factor for the development of ReX is the decrease in the average GND density and the reduction of the GND density gradient between neighboring grains, attributable to the low GND density in both grains. After annealing, the GNDs were heterogeneously distributed across the grains: for some grains, the density decreased to a minimum after 60 min of annealing, while for other grains, it remained the same as in the deformed state (cf. Fig. 4b and c).

3.3. Analysis of the grain size distributions

Experimental histograms of the grain size distribution in the as-deformed state are lognormal with one mode and a maximum at 1.2 μm (Fig. 5a).

A further increase in the annealing duration leads to an increase in the mean grain size and maximum of the grain size distribution as shown in Table 1 and Fig. 5. Thus, pure aluminum subjected to HPTE and annealed at 300 °C exhibits typical recrystallization kinetics for SPD materials. After annealing for 10 and 30 min the primary normal grain growth stage is clearly present, accompanied by a significant drop in dislocation density (Table 1).

With the increase of the annealing time, the grain size distributions apparently become unimodal, which indicates normal grain growth. The dislocations produced during plastic deformation annihilate through the mechanisms of gliding and climbing at the recovery stage, while the rearrangement of dislocations results in the formation of LAGBs and HAGBs structures after 60 min of annealing, as shown in Fig. 6.

4. Phase-field modeling of recrystallization

4.1. Free energy functional

Functional and interfacial contributions. A multicomponent multiphase-field model presented by Nestler et al. [31], which includes the consideration of the interfacial energy variation according to Read–Shockley [32,33] and the interfacial mobility variation according to Humphreys [21], is used to simulate the ReX process. To account for the stored energy in the system, which acts as a bulk driving force for ReX and reduces the deformation-induced dislocations in a system, an additional

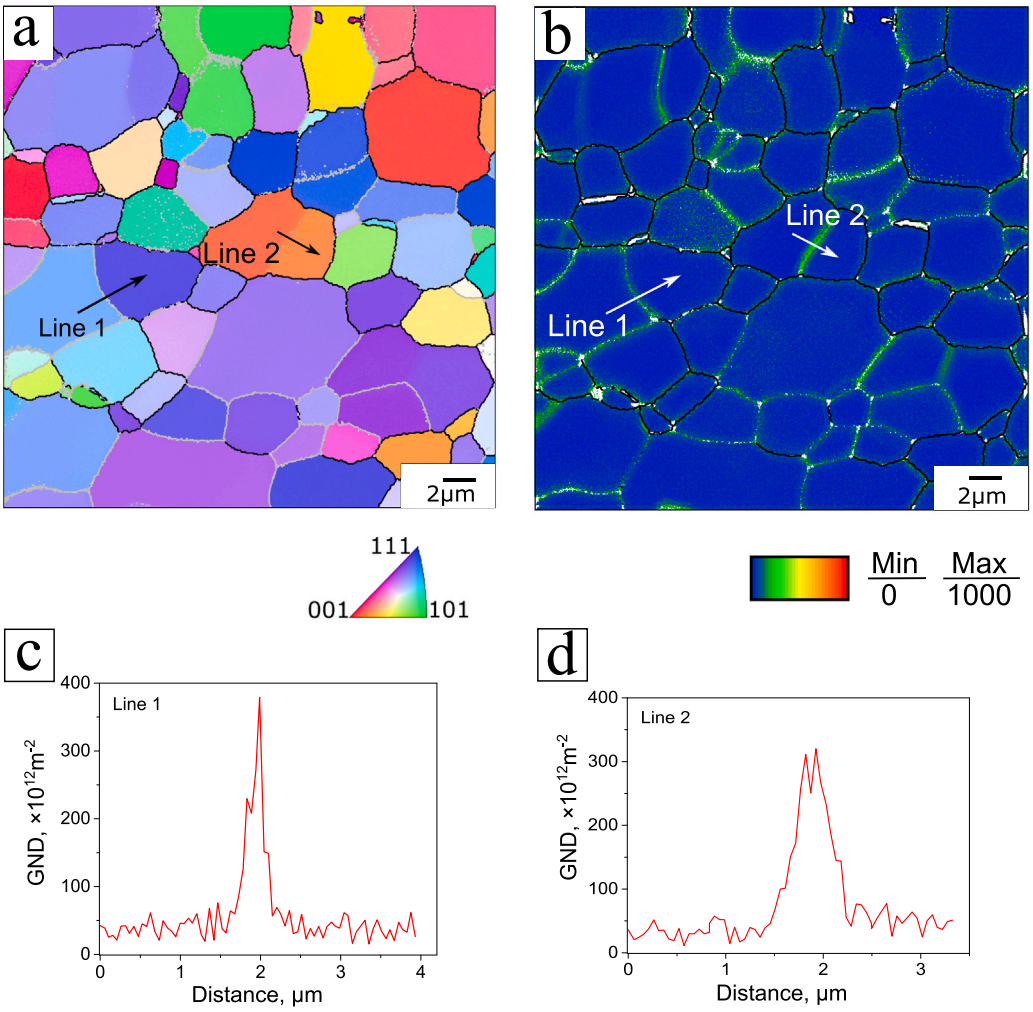

Fig. 6. Microstructure of the HPTE-processed Al after 60 min of annealing at 300 °C. Inverse pole figure maps (a). Geometrically necessary dislocation density distributions (b) are shown in a color-coded map at the scale [$\times 10^{12}\mathrm{m}^{-2}$]. The deformation directions, the standard stereographic triangle, and the GND density scale are shown in the lower part of the figure. HAGBs are indicated by the black lines, LAGBs by the gray lines. GND distributions along the lines 1 and 2 are represented in (c) and (d) accordingly.

bulk energy term is included following the approach of Vondrous et al. [33,34]. Thus, the free energy functional reads as

$$\mathcal{F} = \int_V \underbrace{\varepsilon a(\boldsymbol{\phi}, \nabla\boldsymbol{\phi}) + \frac{1}{\varepsilon}\omega(\boldsymbol{\phi})}_{W_{\mathrm{intf}}} + \underbrace{f_{\mathrm{RX}}(\boldsymbol{\phi}, \rho_d)}_{\overline{W}_{\mathrm{bulk}}} \mathrm{dV}, \tag{2}$$

where W_{intf} denotes the interfacial and $\overline{W}_{\mathrm{bulk}}$ the bulk contribution of the free energy density. The N-tuple of continuous order parameters is referred to as $\boldsymbol{\phi} = \{\phi_1, \ldots, \phi_\alpha, \ldots, \phi_N\}$, where each order parameter, $\phi_\alpha(\boldsymbol{x}, t)$, represents the volume fraction of a particular phase or grain α. Here, each order parameter is identified with a corresponding grain. The interfacial energy density consists of the gradient contribution $\varepsilon a(\boldsymbol{\phi}, \nabla\boldsymbol{\phi})$ and the multi-obstacle type potential $\omega(\boldsymbol{\phi})/\varepsilon$. The thickness of the diffuse interface is proportional to the parameter ε. According to Nestler et al. [31], the gradient energy density is defined as

$$\varepsilon a(\boldsymbol{\phi}, \nabla\boldsymbol{\phi}) = \varepsilon \sum_{\alpha<\beta} \gamma_{\alpha\beta} |\phi_\alpha \nabla\phi_\beta - \phi_\beta \nabla\phi_\alpha|^2, \tag{3}$$

where $\gamma_{\alpha\beta}$ denotes the interfacial energy between the phases/grains α and β. A detailed description regarding the multi-obstacle potential $\omega(\boldsymbol{\phi})$ is given, in Ref. [31,35].

Bulk contribution. The bulk energy density term $\overline{W}_{\mathrm{bulk}}$, which depends on density of geometrically necessary dislocations ρ_d, represents the stored energy of the system and is defined as

$$\overline{W}_{\mathrm{bulk}}(\boldsymbol{\phi}, \rho_d) = W_{\mathrm{bulk}}(\rho_d) \sum_{\alpha}^{N} m_\alpha h(\phi_\alpha), \tag{4}$$

$$W_{\mathrm{bulk}}(\rho_d) = \frac{1}{2}\rho_d G b^2, \tag{5}$$

where G is the shear modulus and b is the Burgers vector [32]. In the present work, $h(\phi_\alpha) = \phi_\alpha$ is used as interpolation function. The phase-inherent storage parameter m_α is related to the conventional theory of the static ReX [36].

4.2. Evolution of the order parameter

Evolution equation. Taking into account the constraint $\sum_\alpha \phi_\alpha = 1$, the evolution equation according to the variational approach of Steinbach and Pezzolla [37] is:

$$\frac{\partial\phi_\alpha}{\partial t} = -\frac{1}{\epsilon\tilde{N}} \sum_{\beta\neq\alpha}^{\tilde{N}} M_{\alpha\beta}(\Theta) \left[\frac{\delta f}{\delta\phi_\alpha} - \frac{\delta f}{\delta\phi_\beta}\right], \quad \forall\phi_\alpha, \alpha = 0, \ldots, \tilde{N}, \tag{6}$$

where $\tilde{N}$ denotes the number of locally active phases. In this context, the variational derivative is used, which reads as follows:

$$\frac{\delta f}{\delta\phi_\alpha} = \frac{\partial f}{\partial\phi_\alpha} - \mathrm{div}\left[\frac{\partial f}{\partial\nabla\phi_\alpha}\right], \tag{7}$$

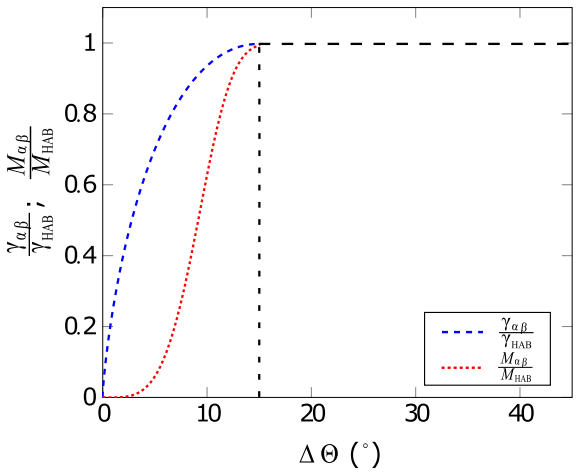

Fig. 7. Interfacial energy and mobility as a function of misorientation of crystal lattices (Eqs. 9 and 10) between two grains for $\gamma^{\mathrm{sim}}_{\mathrm{HAGB}} = 1$ J/m^2 and $M^{\mathrm{sim}}_{\mathrm{HAGB}} = 10^{13}$ m^4/(Js)$^{-1}$. Above a misorientation of $\Delta\Theta_m = 15°$, the value is constant.

where $\nabla\phi_\alpha$ is the gradient of the order parameter ϕ_α and div(·) represents the divergence operator. The volumetric energy densities in interfacial regions can be evaluated such that the deviation from the equilibrium profile is minimized [38]. Then, the evolution equation can be written as

$$\frac{\partial\phi_\alpha}{\partial t} = -\frac{1}{\epsilon\tilde{N}}\sum_{\beta\neq\alpha}^{\tilde{N}} M_{\alpha\beta}\left[\frac{\delta W^{\mathrm{intf}}}{\delta\phi_\alpha} - \frac{\delta W^{\mathrm{intf}}}{\delta\phi_\beta} + \frac{8\sqrt{\phi_\alpha\phi_\beta}}{\pi}\Delta W^{\alpha\beta}_{\mathrm{bulk}}\right]. \tag{8}$$

where $\Delta W^{\alpha\beta}_{\mathrm{bulk}} = \frac{\partial\overline{W}_{\mathrm{bulk}}}{\partial\phi_\alpha} - \frac{\partial\overline{W}_{\mathrm{bulk}}}{\partial\phi_\beta}$, cf., e.g., [38,39].

In the work at hand, the presented MPFM is applied to polycrystalline microstructure obtained by EBSD measurements. Consequently, a coupling with mechanics [40] involving crystal plasticity [41] is not considered due to the numerical cost involved. In this regard, the ReX simulation of a two-dimensional computational domain contains up to $N = 10\,000$ grains. Correspondingly, the evolution of N grains is calculated by N evolution equations of the form as in Eq. (8). To properly account for the reduction in memory requirements, a method for reducing local order parameters is incorporated [23].

Read–shockley model for interfacial energy and mobility. In the work at hand, the interfacial energy $\gamma_{\alpha\beta}$ is a function of the misorientation angle $\Delta\Theta_{\alpha\beta}$ between the grains α and β, which is in accordance with Read and Shockley [32] and reads

$$\gamma_{\alpha\beta}(\Delta\Theta_{\alpha\beta}) = \begin{cases} \gamma_{\mathrm{HAGB}}\frac{\Delta\Theta_{\alpha\beta}}{\Delta\Theta_m}\left(1 - \ln\frac{\Delta\Theta_{\alpha\beta}}{\Delta\Theta_m}\right), \Delta\Theta_{\alpha\beta} < \Delta\Theta_m \\ \gamma_{\mathrm{HAGB}}, \qquad \text{else.} \end{cases} \tag{9}$$

In this context, γ_{HAGB} is the interfacial energy of the HAGB. The transition from the LAGB to the HAGB takes place at $\Delta\Theta_m = 15°$. Consequently, according to Humphreys [21], the mobility between the phases α and β can be written as

$$M_{\alpha\beta}(\Delta\Theta_{\alpha\beta}) = \begin{cases} M_{\mathrm{HAGB}}\left[1 - \exp\left(-5\left(\frac{\Delta\Theta_{\alpha\beta}}{\Delta\Theta_{\mathrm{m}}}\right)^4\right)\right], \text{else} \\ M_{\mathrm{HAGB}}, \qquad \text{for } \Delta\Theta_{\alpha\beta} > \Delta\Theta_{\mathrm{m}}, \end{cases} \tag{10}$$

where M_{HAGB} models the mobility of the HAGB. In particular, for small misorientations, both the mobility and the interfacial energy, nearly vanish, as shown in Fig. 7

In the present work, the Read–Shockley model is used for simulation by extending it to all kinds of grain boundaries such as [110] tilt or twist grain boundaries, which is a significant simplification. Furthermore, it is assumed that the energy remains constant for a misorientation angle

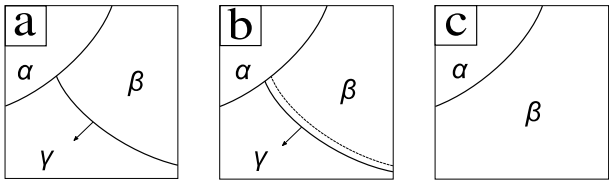

Fig. 8. Schematic representation of grain boundary movement at varying dislocation densities. The dislocation density values between the α, β, and γ grains are interrelated: $m_\alpha = m_\gamma = 1$, $0 < m_\beta < 1$ (a); $\Delta\Theta_{\alpha\beta} < 2°$, $M_{\alpha\beta} \approx 0$, so no movement between α and β (b); $\Delta\Theta_{\beta\gamma} \gg \Delta\Theta_{\alpha\beta}$ Movement of β towards γ (c) migration of β grain boundary towards the γ grain, (b), the grain boundary has migrated towards the γ grain (c) (this schematic example is demonstrated in simulated structures in Fig. 13).

that exceeds the introduced threshold value Θ_{max}, cf., e.g., Vondrous et al. [33].

Schematic illustration of applied model. For illustrative purpose, the basic scheme of grain boundary motion is presented in Fig. 8. The direction and velocity of grain boundaries in MPFM depend on the dislocation density distribution and curvature. The movement of grain boundaries in the vicinity of a grain boundary triple junction with different GND densities is illustrated in Fig. 8a. The dislocation density values between the α-, β-, and γ grains are identical, whereas the γ grain exhibits a markedly higher dislocation density. As illustrated in Fig. 8b, the grain boundary undergoes a movement. The orientational remnants of the growing grain situated between the γ- and β- grains migrate towards the γ grain. Upon movement, the boundaries of grain orientation γ undergo a complete transformation into grain orientation β (Fig. 8c). In the event that the grain in question exhibits small-angle misorientations, all points within the grain are equally attached to the growing grain.

A detailed description of the grain boundary motion as an example of the small area of the microstructure is represented in Appendix.

5. Multiphase-field simulation studies

5.1. Objective and simulation setup

Objective of the simulation studies. Simulation studies are performed with the multiphase and multiphysics framework Pace3D [23]. The simulations discussed below provide insight into the microstructural changes during CReX that determine the overall crystallization kinetics. They are carried out on the microstructure provided by the experimentally determined EBSD-scans. Thus, no simplification regarding the initial orientation of the considered grains is taken into account. Furthermore, the initial stored energy is calculated from the measured dislocation density according to Eq. (4). The MPMF simulations account for the minimization of the free energy. The resulting changes in stored energy are compared to the experimentally measured GND density at the corresponding time step.

Simulation set-up and boundary conditions. The evolution equation of the order parameter, given by Eq. (8), is discretized regarding a Cartesian grid. In this context, an equidistant grid is used with quadratic cells with a width of 0.33 µm. Thus, the overall simulation domain consists of 1630 × 1288 cells. It is solved by application of an explicit time integration scheme, implemented within the in-house software suite Pace3D, regarding a time step $\Delta t_{sim} = 3$ s. Fig. 10a presents a representative map of the initial Al structure, imported from the EBSD scanned map. In this regard, both, the orientation as well as the grain boundaries are directly imported to Pace3D. Regarding the order parameter, the Neumann boundary condition $\left(\partial W^{\mathrm{intf}}/\partial\nabla\phi_\alpha\right)\cdot\boldsymbol{n} = 0$, $\forall\, \boldsymbol{x} \in \mathcal{V}_t^{\mathrm{N}}$ has to be fulfilled.

Remark on nucleation. In the initial microstructure, which was obtained through experimental means, all of the grains were set as nuclei with equal potential for growth. Since this work is mainly concerned with CReX processes in aluminum, classical nucleation theory, as known from various solid-state transformation processes in other alloy systems, will not provide a reliable basis for the phase-field simulations [42,43]. This is the case because recrystallization occurs due to low driving forces caused exclusively by stored energy [16], due to deformation, in contrast to high driving forces that occur, for example, in solidification processes or solid-state precipitation [31]. Apart from that, the differences in interfacial energies, according to the aforementioned Read–Shockley relation, are very high and thus favor the high-angle grain boundary migration [6]. Furthermore, it seems unlikely that thermal fluctuations themselves could form defect-free regions within a high-angle grain boundary network. Hence, it is likely that the nuclei that form new recrystallized grains do not emerge during the annealing process but are already present in the deformed state before annealing sets in. In fact, there are three well-known recrystallization nucleation models in literature [44]. Beck and Sperry [45] identify the migration of pre-existing HAGB into the interior of neighboring highly strained grains as a main mechanism. The Cahn–Cottrell [46] model, based on the models of Beck [45] and Cahn [47], considers grains and LAGBs surrounding regions of low dislocation density. A formed or pre-existing grain with LAGB can grow at the expense of neighboring grains by thermally assisted low-angle grain boundary migration, resulting in a reduction of stored energy, due to the elimination and rearrangement of microstructural defects. Sandström et al. [48] as well as Varma and Willits [49] and Blum et al. [50] observed that the behavior of growth in grains with LAGBs in pure aluminum, at elevated temperatures from 300 to 400 °C, matches the conditions of the experimental part in this work.

For this reason, the selection of nucleation is primarily aimed at capturing these mechanisms. The third model presented by Boas et al. [51] accounts for the coalescence effects of grains containing LAGBs, which is a viable approach for lower annealing temperatures (below 0.65 T_m) [48,52].

In this work, we introduce and apply a geometrical criterion for nucleation: nucleation is driven solely by the size of the grains, without the use of a specific theoretical nucleation criterion. Nucleation depends on the size of the grains with LAGBs and the misorientation of the grains with LAGBs. Experimentally, grains LAGBs wich diameters smaller than 100 nm are considered nuclei candidates if their corresponding grain boundaries exhibit a misorientation of at least 2 degrees. The size threshold of 100 nm is based on experimental observations, where grains with LAGBs smaller than this size tend to disappear after short annealing times (10 min). The misorientation threshold of 2 degrees reflects the typical minimum detectable angle for low-angle grain boundaries (LAGBs) using an EBSD detector under standard operating conditions. For these identified grains with LAGBs, we assume the grain boundary mobility factor, m_α, to be zero.

Once a cell is fully recrystallized, the stored energy becomes zero. Consequently, $\overline{W}_{\text{bulk}}$ decreases as the recrystallizing phase or grain grows.

Averaged dislocation density from simulations. The applied model accounts for the experimentally measured dislocation density, which is present after the HPTE process, in order to formulate the stored energy. It is anticipated that the SE will be reduced during the simulation, reflecting the characteristic of the ReX process and, thus, the reduction of the dislocation density. For a subsequent comparison between experiments and simulations, the averaged dislocation density $\overline{\rho}_d$ is calculated as

$$\overline{\rho}_d = \frac{1}{A}\int_A \rho_d \, da \tag{11}$$

with the dislocation density distribution ρ_d from the stored energy formulation stated in Eq. (5), and A denoting the area of the simulation domain. This methodology enables the calculation of the averaged dislocation density for any simulated time step.

Table 2
Parameters for Pace3D simulation.

γ_{HAGB} (J m^{-2})	M_{HAGB} (m^4(Js)$^{-1}$)
0.3	5×10^{-13}

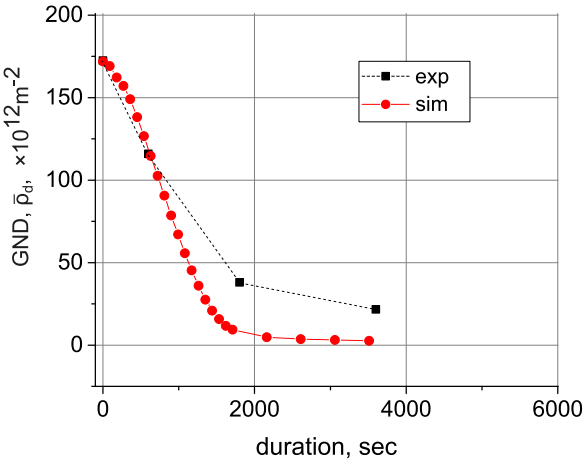

Fig. 9. Evolution of the average simulated and experimental GND density values.

Considered parameters. The value of surface energy $\gamma_{\text{HAGB}} = 0.3$, J/m^2 taken to be close to the experimentally obtained value of $\gamma^{\text{sim}}_{\text{HAGB}} = 0.324$ J/m^2 [53] in pure aluminum at 300 °C. Experimental evaluations in Al-0.05%Si enabled an increase in the range of LAGBs misorientations [54], providing a value for the saturation of the mobility $M^{\text{exp}}_{\text{HAGB}} = 5\times10^{-13}$ m^4(Js)$^{-1}$, which was used for the calculation. Values of $\gamma^{\text{sim}}_{\text{HAGB}}$ and $M^{\text{sim}}_{\text{HAGB}}$ obtained from the Pace3D simulations are given in Table 2.

The dimensionless value of the discrete time step per each simulation cycle is tied to physical time under given calculation conditions. In this correlation, we can scale the simulation step by real annealing time as $\Delta t_{sim} = N_f \times \Delta t_{real}$, where N_f represents the number of calculation steps.

Another assumption is that above a high-angle grain boundary threshold $\Theta_{\max}$, the surface energy remains constant [33]. The saturation level in the simulations reached by the M parameter is the upper boundary.

5.2. Results from simulation studies

Average GND density. The GND density obtained from the MPFM simulations according to Eq. (5) is represented by the red distribution in Fig. 9. For selected simulation times, the results are represented by red dots. After a short nonlinear decay, an almost linear decrease of the averaged dislocation density can be observed. After about 1500 s, this linear decrease transitions to a saturation behavior. From 1800 s on, a steady state of the averaged dislocation density is observed.

The results of the quantitative analysis of the simulated maps are presented in Table 3. It is compared to the experimentally measured change of the GND in Fig. 10.

Already at the initial stage of the simulation ($t_{sim} = 30$ s), the value of GND decreases quickly, which is reflected in a sharp decrease in the number of storage energy aggregates. After $t_{\text{sim}} = 30$ s and $t_{\text{sim}} = 300$ s, the GND falls faster than at the beginning stage. This demonstrates the change in the driving force for the recrystallization process and can be analyzed in connection with the change in the grain size (Table 3).

Grain structure. The resolved microstructures, obtained by the MPFM simulations, are visualized using the same OIM TSL software as was applied for the experimental OIM maps and are represented in Fig. 10a–d. The changes in the shape and orientation of the grains are analyzed

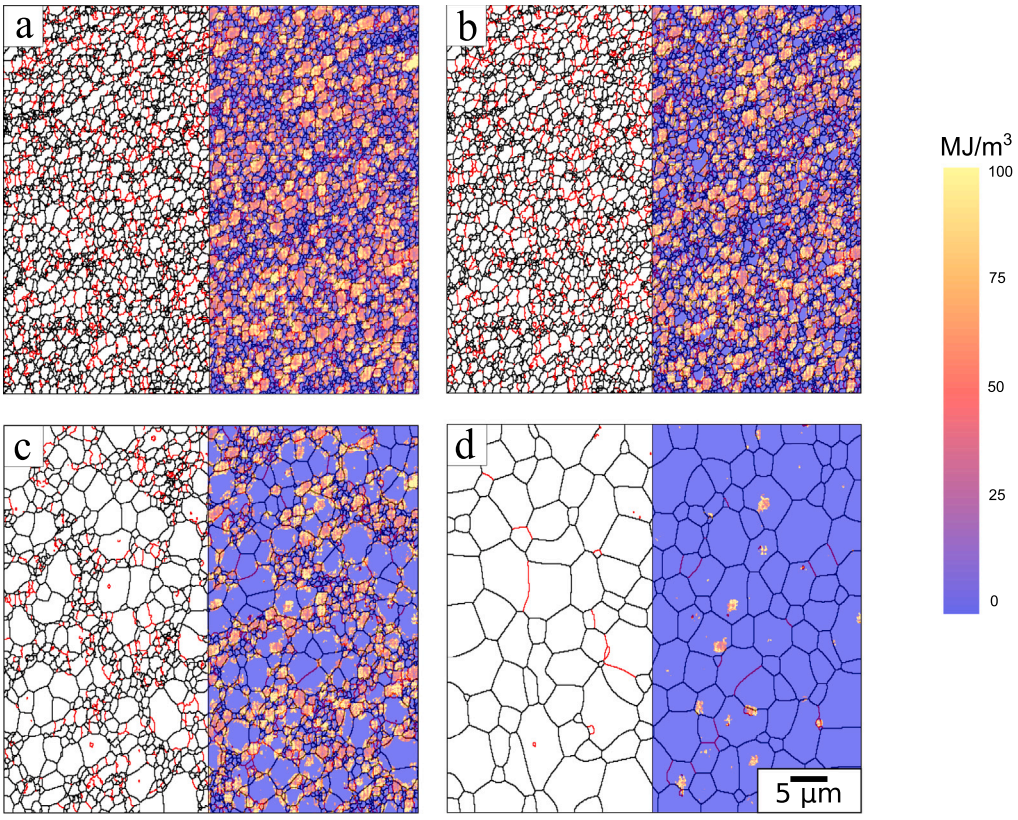

Fig. 10. Grain boundary network of the simulated structures of HPTE-processed Al (left) imported initial structure (a), after t_{sim} = 10 min (b), t_{sim} = 30 min (c), t_{sim} = 60 min (d) of PACE3D simulation time. The stored energy distribution is shown on the right side of (a–d). Again, the black lines refer to the HAGBs, while red lines refer to the LAGBs.

Table 3
Microstructure parameters simulated with PACE3D.

t_{sim} (s)	D^a (µm)	Θ_{sim} (°)	$\bar{\rho}_d^{sim}$ ($\times 10^{12}$ m^{-2})
init	1.63	33.5	173.8
30	1.65	33.0	172.4
60	1.67	33.0	170.8
180	1.73	33.2	162.6
300	1.8	33.3	154.1
600	2.3	33.8	118.8
900	2.7	34.2	78.8
1200	3.2	34.7	40.3
1800	4.7	37.2	8.4
2100	5.2	38.2	5.8
3600	5.5	38.6	2.5

[a] Value of D is indicated for the 1st mode in case maps are characterized by the bimodal D size distribution.

using the grain boundaries network of the modeled structures, displayed on the left side of the structures in Fig. 10. On the right side of the modeled structures in Fig. 10, the distribution of the SE in the structure is depicted. The distribution of SE in the simulated structures, both initially and after different numbers of simulation steps, is highly heterogeneous. Heterogeneous distribution of SE in the structure led to the formation of local areas where most of the sites of storage energy aggregates are clearly marked by the orange, red, and yellow colors on the SE distribution maps (Fig. 10b–d).

A heterogeneous growth kinetics can be observed from the simulated microstructure evolution, depicted in Fig. 10. in this context, after t_{sim} = 150 s (Fig. 10b and c), some grains in the structure of Al stayed small, while some grains became notably larger. Considering the grain size distribution histograms (Fig. 11), until t_{sim} = 600 s of the simulation, the simulated structure is characterized by a lognormal distribution. With an increasing duration of simulation time, the position of the main peak on the histogram is shifted to the area of the higher values. The lognormal character of the grain size distribution indicates the normal grain growth kinetics of the simulated recrystallization, which is completely matched with experimentally obtained ReX kinetics.

After t_{sim} = 600 s, the grain size distribution of the simulated structure appears much more homogeneous compared to the structure after t_{sim} = 900 s (Fig. 10(d) and (c)). The areas of the small grains in the grain boundary network are clearly matched with the places of high concentration of stored energy aggregates in the structure (left and right sides in Fig. 10c). The strong reduction of the GND in general and disappearance of the storage energy aggregates after t_{sim} = 3600 s are accompanied by significant coarsening of the grains size in the grain boundary network (Fig. 10d).

6. Discussion

6.1. GND distribution evolution during annealing

Averaged GND distribution during rex. In Fig. 9 four experimentally obtained averaged dislocation density values are depicted over the recrystallization time. Both distributions from simulation and experiments show a significant decrease at the beginning with a saturation to a steady-state behavior. The average dislocation density in the simulations saturates as it approaches a vanishing dislocation density. This fit to the experimental dislocation density is due to the imposed grand stage dislocation density value used in the nucleation criterion. This difference can be explained by the applied multiphase-field method.

Local evolution of stored energy. Considering the changes in GND distribution in the experimental structures before (Fig. 2b–d) and after 60 min of annealing time (Fig. 6b–d), it can be noted that the highest GND density is observed in the area close to the HAGBs. This

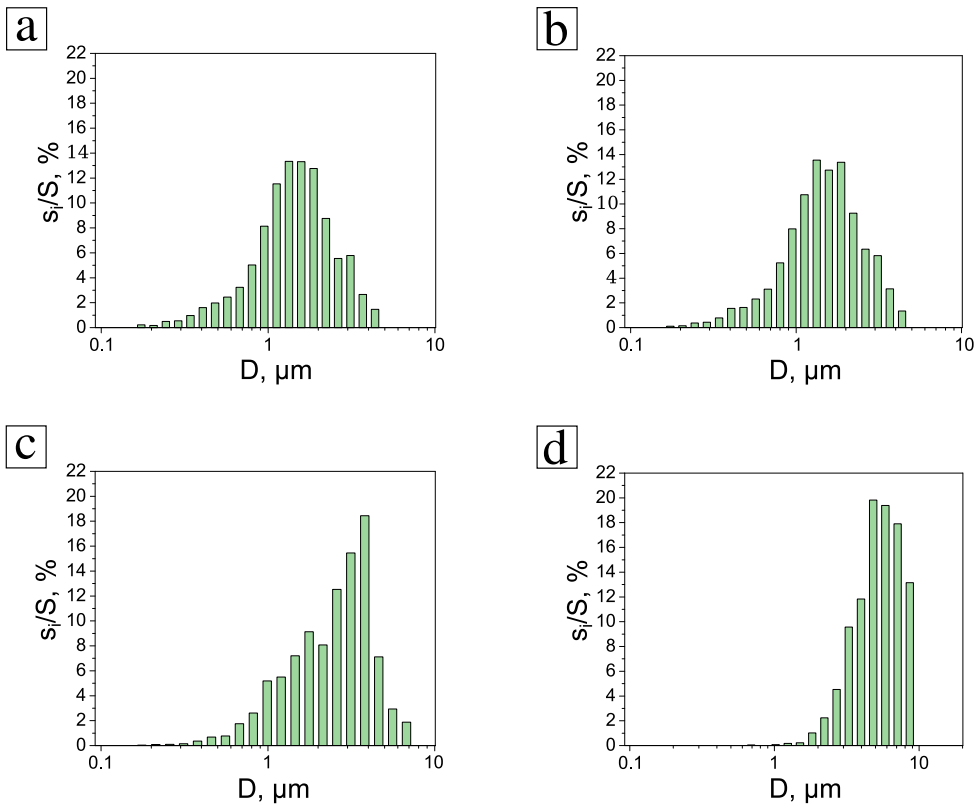

Fig. 11. Grain size distributions D by specific area s_i/S of HPTE-processed Al: (a) imported initial structure, after t_{sim} = 10 min (b), t_{sim} = 30 min (c), and t_{sim} = 60 min (d) by PACE3D simulation.

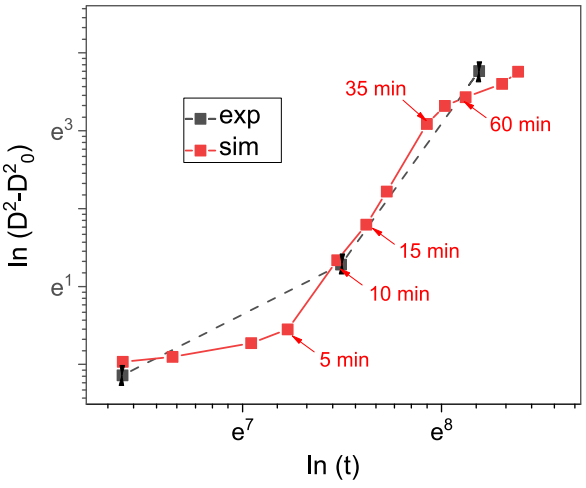

Fig. 12. Experimental and simulated grain structure coarsening kinetics, $\ln(D^2 - D_0^2)$, as a function of annealing time $\ln(t)$.

indicates well-known mechanisms of dislocation annihilation, recovery, and nucleation of recrystallization [6].

In context, regarding the simulations, it can be observed that as the grains grow, the stored energy aggregation sites (SEAS) are not dominated at the HAGBs, but are also present within the grains. Moreover, at a later stage of the simulation of the grain growth, e.g., after 60 min, the SEAS are either aggregated inside a grain or at one HAGB, but not distributed along the HAGBs, at it is observed in the experiments, depicted in Fig. 6.

This discrepancy in experimental and simulated structures can be explained in terms of MPFM formalism, which does not consider dislocation density evolution and formation of additional GBs. Thus, the character of energy minimization differs from the experimentally observed recovery mechanism via the substructure formation and dislocation movement to the HAGBs.

The multiphase-field method states that the sum of interfacial and bulk free energy density is minimized. Consequently, bulk and interfacial driving forces are associated with the microstructure evolution. In this regard, both the mobility $M_{\alpha\beta}$ and interfacial energy $\gamma_{\alpha\beta}$ are highly dependent on the misorientation angle, due to the Read–Shockley model. While the mobility affects the overall microstructure evolution, the interfacial free energy only affects the interfacial driving force. The bulk driving force is defined by means of the SE in terms of the experimentally measured GND density. Consequently a reduction of the SE reflects a reduction of the GND density as illustrated by Table 3. In regions that are completely free of SE across the grain boundary, the grain boundary evolution is given by the interfacial driving force. However, the simplification of the GND density evolution as the minimization of SE through the GB motion allows to extract the clear effect of the GB motion on the ReX and grain growth kinetics.

Experimentally, the decrease of the average GND density after 10 min of annealing is accompanied by the change of the ReX stage to grain growth. A similar change from ReX to grain growth is obtained for the simulated structures after the change of the stable state of the SE level, which is accompanied by the normal grain growth (Table 2).

6.2. *Recrystallization kinetics analysis*

Based on the experimental and simulated values of D (Table 1 and 3), the recrystallization kinetics are plotted in Fig. 12. Thereby, Eq. (1) is used to plot $ln(D^2 - D_0^2)$ over $ln(t)$, yielding three points for the experimentally determined averaged GND density over time.

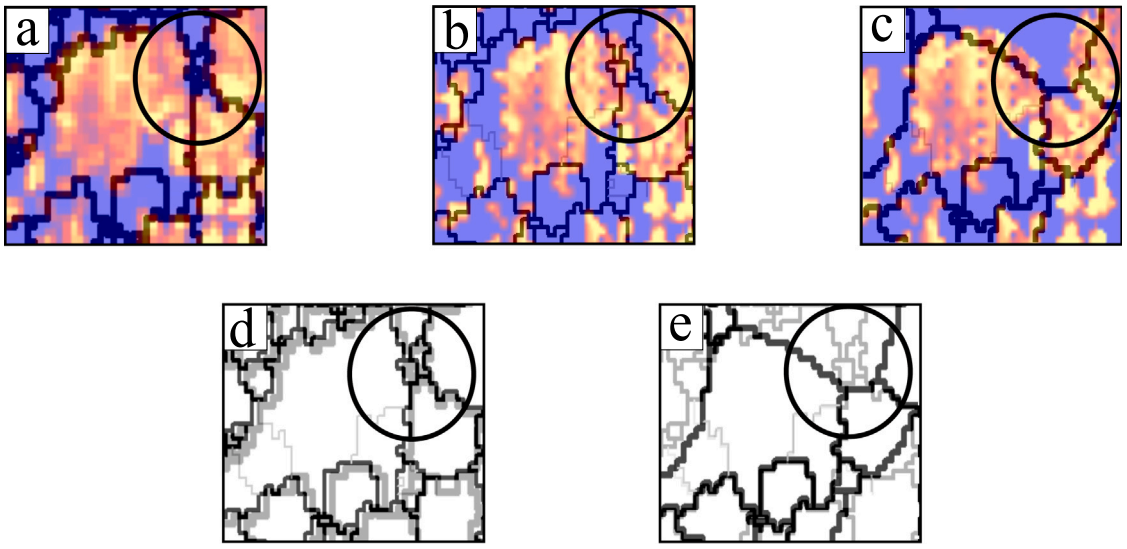

Fig. 13. The grain boundaries network after various simulation time of ReX $t_{sim} = 0\,\mathrm{s}$ (a), $30\,\mathrm{s}$ (b), $900\,\mathrm{s}$ (c), $0\,\mathrm{s} + 30\,\mathrm{s}$ (d), $30\,\mathrm{s} + 900\,\mathrm{s}$ (e). $\overline{\rho}_d^{\,\mathrm{sim}}$ in (a), (b), (c) is represented in the same color scheme as in Fig. 10. In the area delineated by the circle, the boundaries exhibit a clear tendency to movement in a direction with a larger value of SE. The gray lines in (d) and (e) represent the HAGBs in relation to (a) and (b), respectively. The black lines in(d) and (e) represent HAGBs with (b) and (c), respectively.

In this context, two distinct kinetics are observed in the experiment, characterized by different slopes of the interpolation between the measured points. The first kinetics occurs in the interval of 10 to 30 min with a slope $n_1 = 1.3$, while the second one occurs in the interval between 30 and 60 min with $n_2 = 3.6$. Consequently, regarding the UFG aluminum, a faster grain growth is observed within $t \in [30, 60]$ min than for the fine-grained aluminum for $t \in [10, 30]$ min. Both slopes n_1 and n_2 are higher than the slope that is documented in literature [55,56] for conventionally deformed aluminum, for which $n \approx 1$ holds. The results of the simulation are also shown in Fig. 12, which shows good agreement with the experimentally determined values.

In addition, since results for an arbitrary time step can be extracted from the simulations, they provide insight into the behavior between the experimentally obtained data. Also from the simulational results, two kinetics regimes can be observed. Similar to the experimental observation, a less pronounced grain growth is observed in the first interval compared to the second interval. This tendency of the lowering of the ReX and grain growth kinetic for the higher grain size follows the general trend that a fine-grained material will recrystallize more rapidly than a coarse-grained material [6].

7. Conclusion

In this work, the ReX process of UFG aluminum during annealing is investigated by both simulations and experiments. In order to simulate the ReX process, an MPFM is applied that is based on the experimentally measured GND density as well as the measured misorientation of the GBs. It is combined with a nucleation criterion that is of purely geometric nature in that it accounts for the size of the subgrains and their misorientation. The model captures a successive change in the driving force of recrystallization due to a decrease of the SE and the minimization of surface energy, reflecting two recrystallization mechanisms. This approach allows the generation of the digital twin of the ReX kinetics. It accounts for the dependency of the grain boundary mobility on the misorientation of the grains. The evolution of the GND density results from the minimization of the SE without explicit consideration of the dislocation density dynamics. Nevertheless it allows to replicate the decrease of the averaged GND density both quantitatively and qualitatively. Moreover, the ReX kinetics obtained by the simulations is in good agreement with the kinetics associated with the experiments. Due to the nature of the digital twin, it yields additional insight into the kinetics of ReX, where experiments were not available. Moreover, the grain size distributions obtained from simulations and experiments, that capture the grain growth in a statistical manner, show the same tendency. Both data exhibit a lognormal distribution, with a shift of the distributed center towards larger grains over the annealing time. By combining experimental observations with computational modeling, this integrated approach elucidates the fundamental mechanisms underlying the recrystallization and grain growth behavior of SPD-processed aluminum. With regard to the continuous ReX in deformed pure *fcc* metals, it has been demonstrated that the heterogeneous distribution of the dislocation density obtained and measured inside the grains in as deformed UFG state is significantly reduced. This is a consequence of the formation and growth of crystals with low dislocation density. The simulations based on the MPFM and carried out in the in-house software suite PACE3D allow for predicting the kinetics of recrystallization, as well as the GND reduction for the application to the softening prediction.

CRediT authorship contribution statement

Olena Abramova: Writing – review & editing, Writing – original draft, Methodology, Formal analysis, Conceptualization. **Dayan Nugmanov:** Writing – review & editing, Methodology, Investigation, Data curation. **Daniel Schneider:** Writing – review & editing, Supervision, Conceptualization. **Andreas Prahs:** Writing – review & editing, Supervision. **Tobias Mittnacht:** Writing – review & editing, Software, Methodology. **Julia Ivanisenko:** Writing – review & editing, Validation, Supervision. **Brigitte Baretzky:** Project administration, Funding acquisition. **Britta Nestler:** Writing – review & editing, Supervision, Funding acquisition.

Declaration of competing interest

The authors declare that they have no known competing financial interests or personal relationships that could have appeared to influence the work reported in this paper.

Acknowledgments

The authors gratefully acknowledge financial support of the research through the programmes "Virtual Materials Design" VirtMat project no.P05 and "Material Systems Engineering (MSE)" of the Helmholtz association. Data and data processing are provided within

the KNMFi and MDMC initiatives (no. 43.31.01) of the Helmholtz association through the research data infrastructure KADI4MAT https://kadi.iam.kit.edu.

Appendix

The grain boundary motion in the small area of the microstructure is considered. In Fig. 13 the toy example of one experimentally obtained structure in an as-received deformed state (a), after $t_{sim} = 30\,s$ (b) and $t_{sim} = 900\,s$ (c) is represented. HAGBs are marked by thick black lines, and LAGBS are marked by thin black lines. The SE distribution is shown according to the color legend given in Fig. 10. In the initial state, we can see the big grain with a high SE, and therefore GND density surrounded by the small dislocation-free small grains (Fig. 13a). After short-time annealing $t_{sim} = 30\,s$ the SE value inside the big grain reduced, however, the HAGBs does not show a significant movement. Fig. 13d contains a superimposed grain boundary network in the initial state marked by black lines and a grain boundary network after $t_{sim} = 30\,s$ marked by gray lines. As we can see, the position of most of the grain boundaries before and after annealing during $t_{sim} = 30\,s$ is matching. Next, after $t_{sim} = 900\,s$ (Fig. 13c) the distribution of SE is still the same as that after short-time annealing (Fig. 13b). However, the positions of the small grains after $t_{sim} = 900\,s$ are changed significantly.

Let us consider the motion of HAGBs in a small region inside the circle depicted in Fig. 13a–c. In the initial state and after $t_{sim} = 30\,s$ two small grains are completely placed inside the circle surrounded by four big grains. After $t_{sim} = 900\,s$, only four big grains remain partially inside the circle. The two small grains disappeared, resulting from the HAGB motion from the big grain at the top that was dislocation-free in its initial state. Superimposing the grain boundary networks after $t_{sim} = 30\,s$ (gray lines) and $t_{sim} = 900\,s$ (black lines) in Fig. 13d demonstrates the shifting of HAGBs. Two small grains were joined to the big one as a result of the HAGBs motion from the area with low SE to the area with high SE.

Data availability

Data will be made available on request.

References

[1] A. Belyakov, K. Tsuzaki, H. Miura, T. Sakai, Effect of initial microstructures on grain refinement in a stainless steel by large strain deformation, Acta Mater. 51 (3) (2003) 847–861.

[2] A. Belyakov, Y. Kimura, K. Tsuzaki, On structural mechanism of continuous recrystallization in ferritic stainless steel after large strain processing, Mater. Sci. Forum 503–504 (2006) 323–328.

[3] N. Hansen, X. Huang, M. Møller, A. Godfrey, Thermal stability of aluminum cold rolled to large strain, J. Mater. Sci. 43 (18) (2008) 6254–6259.

[4] N. Kamikawa, X. Huang, N. Tsuji, N. Hansen, Strengthening mechanisms in nanostructured high-purity aluminium deformed to high strain and annealed, Acta Mater. 57 (14) (2009) 4198–4208.

[5] W. Burton, N. Cabrera, F. Frank, N. Mott, The growth of crystals and the equilibrium structure of their surfaces, Phil. Trans. R. Soc. A 243 (866) (1951) 299–358.

[6] F. Humphreys, M. Hatherly, Recrystallization and Related Annealing Phenomena, Elsevier, 2012.

[7] T. Orlova, N. Skiba, A. Mavlyutov, M. Murashkin, R. Valiev, M. Gutkin, Hardening by annealing and implementation of high ductility of ultra-fine grained aluminum: experiment and theory, Rev. Adv. Mater. Sci. 57 (2) (2018) 224–240.

[8] T. Orlova, T. Latynina, A. Mavlyutov, M. Murashkin, R. Valiev, Effect of annealing on microstructure, strength and electrical conductivity of the pre-aged and HPT-processed Al-0.4Zr alloy, J. Alloys Compd. 784 (2019) 41–48.

[9] P. Feltham, Grain growth in metals, Acta Metall. 5 (2) (1957) 97–105.

[10] P. Rios, Abnormal grain growth in materials containing particles, Acta Metall. Mater. 42 (3) (1994) 839–843.

[11] J. Burke, D. Turnbull, Recrystallization and grain growth, Prog. Met. Phys. 3 (1952) 220–292.

[12] N. Louat, On the theory of normal grain growth, Acta Metall. 22 (6) (1974) 721–724.

[13] C. Krill III, L. Chen, Computer simulation of 3-D grain growth using a phase-field model, Acta Mater. 50 (12) (2002) 3059–3075.

[14] S. Kim, D. Kim, W. Kim, Y. Park, Computer simulations of two-dimensional and three-dimensional ideal grain growth, Phys. Rev. E 74 (6) (2006) 061605.

[15] R. Brandt, W. Graupner, K. Luecke, Normal and abnormal grain growth and particularly the behaviour of large and small grains as predicted by simulations on the basis of the statistical model, in: Materials Science Forum, Vol. 204, Trans Tech Publ, 1996, pp. 295–302.

[16] M. Winning, A. Rollett, G. Gottstein, D. Srolovitz, A. Lim, L. Shvindlerman, Mobility of low-angle grain boundaries in pure metals, Phil. Mag. 90 (22) (2010) 3107–3128.

[17] G. Zahid, Y. Huang, P. Prangnell, Microstructure and texture evolution during annealing a cryogenic-SPD processed Al-alloy with a nanoscale lamellar HAGB grain structure, Acta Mater. 57 (12) (2009) 3509–3521.

[18] O. Mishin, A. Godfrey, D. Jensen, N. Hansen, Recovery and recrystallization in commercial purity aluminum cold rolled to an ultrahigh strain, Acta Mater. 61 (14) (2013) 5354–5364.

[19] C. Yu, P. Sun, P. Kao, C. Chang, Evolution of microstructure during annealing of a severely deformed aluminum, Mater. Sci. Eng. A 366 (2) (2004) 310–317.

[20] A. Mavlyutov, A. Bondarenko, M. Murashkin, E. Boltynjuk, R. Valiev, T. Orlova, Effect of annealing on microhardness and electrical resistivity of nanostructured SPD aluminium, J. Alloys Compd. 698 (2017) 539–546.

[21] F. Humphreys, A unified theory of recovery, recrystallization and grain growth, based on the stability and growth of cellular microstructures—I. The basic model, Acta Mater. 45 (10) (1997) 4231–4240.

[22] H. Hakan, Approaches to modeling of recrystallization, Metals 1 (1) (2011) 16–48.

[23] J. Hötzer, A. Reiter, H. Hierl, P. Steinmetz, M. Selzer, B. Nestler, The parallel multi-physics phase-field framework Pace3D, J. Comput. Sci. 26 (2018) 1–12.

[24] Y. Ivanisenko, R. Kulagin, V. Fedorov, A. Mazilkin, T. Scherer, B. Baretzky, H. Hahn, High pressure torsion extrusion as a new severe plastic deformation process, Mater. Sci. Eng. A 664 (2016) 247–256.

[25] R. Kulagin, Y. Beygelzimer, Y. Estrin, Y. Ivanisenko, B. Baretzky, H. Hahn, A mathematical model of deformation under high pressure torsion extrusion, Metals 9 (3) (2019).

[26] F. Humphreys, Characterisation of fine-scale microstructures by electron backscatter diffraction (EBSD), Scr. Mater. 51 (8) (2004) 771–776.

[27] N. Brook, The equivalent core diameter method of size and shape correction in point load testing, Int. J. Rock Mech. Min. Sci. Geomech. Abstr. 22 (2) (1985) 61–70.

[28] A.J. Schwartz, M. Kumar, B.L. Adams, D.P. Field, Electron Backscatter Diffraction in Materials Science, Springer New York, NY, 2009.

[29] M. Calcagnotto, D. Ponge, E. Demir, D. Raabe, Orientation gradients and geometrically necessary dislocations in ultrafine grained dual-phase steels studied by 2D and 3D EBSD, Mater. Sci. Eng. A 527 (10–11) (2010) 2738–2746.

[30] P. Prangnell, J. Hayes, J. Bowen, P. Apps, P. Bate, Continuous recrystallisation of lamellar deformation structures produced by severe deformation, Acta Mater. 52 (11) (2004) 3193–3206.

[31] B. Nestler, H. Garcke, B. Stinner, Multicomponent alloy solidification: Phase-field modeling and simulations, Phys. Rev. E 71 (4) (2005) 041609.

[32] W. Read, W. Shockley, Dislocation models of crystal grain boundaries, Phys. Rev. 78 (3) (1950) 275–289.

[33] A. Vondrous, M. Reichardt, B. Nestler, Growth rate distributions for regular two-dimensional grains with read–shockley grain boundary energy, Modelling Simul. Mater. Sci. Eng. 22 (2) (2014) 025014.

[34] A. Vondrous, P. Bienger, S. Schreijäg, M. Selzer, D. Schneider, B. Nestler, D. Helm, R. Mönig, Combined crystal plasticity and phase-field method for recrystallization in a process chain of sheet metal production, Comput. Mech. 55 (2) (2015) 439–452.

[35] J. Hötzer, O. Tschukin, M. Said, M. Berghoff, M. Jainta, G. Barthelemy, N. Smorchkov, D. Schneider, M. Selzer, B. Nestler, Calibration of a multi-phase field model with quantitative angle measurement, J. Mater. Sci. 51 (4) (2016) 1788–1797.

[36] O. Abramova, A. Prahs, D. Schneider, B. Nestler, The effect of subgrain mobility on recrystallization kinetics: phase-field simulation study, J. Phys. Conf. Ser. 2635 (1) (2023) 012032.

[37] I. Steinbach, F. Pezzolla, A generalized field method for multiphase transformations using interface fields, Physica D 134 (4) (1999) 385–393.

[38] I. Steinbach, Phase-field models in materials science, Modelling Simul. Mater. Sci. Eng. 17 (7) (2009) 073001.

[39] E. Schoof, Chemomechanische Modellierung der Wärmebehandlung von Stählen mit der Phasenfeldmethode (Ph.D. thesis), Karlsruher Institut für Technologie (KIT), 2020.

[40] T. Kannenberg, L. Schöller, A. Prahs, D. Schneider, B. Nestler, Microstructure evolution accounting for crystal plasticity in the context of the multiphase-field method, Comput. Mech. (2023 (online first)).

[41] A. Prahs, L. Schöller, F.K. Schwab, D. Schneider, T. Böhlke, B. Nestler, A multiphase-field approach to small strain crystal plasticity accounting for balance equations on singular surfaces, Comput. Mech. 73 (4) (2024) 773–794.

[42] R. Doherty, D. Hughes, F. Humphreys, J. Jonas, D. Jensen, M. Kassner, W. King, T. McNelley, H. McQueen, A. Rollett, Current issues in recrystallization: a review, Mater. Sci. Eng. A 238 (2) (1997) 219–274.
[43] P. Rios, F.S. Jr., H. Sandim, R. Plaut, A. Padilha, Nucleation and growth during recrystallization, Mater. Res. 8 (3) (2005) 225–238.
[44] P. Rios, Abnormal grain growth development from uniform grain size distributions, Acta Mater. 45 (4) (1997) 1785–1789.
[45] P.A. Beck, P.R. Sperry, Strain induced grain boundary migration in high purity aluminum, J. Appl. Phys. 21 (2) (1950) 150–152.
[46] A. Cottrell, Progress in metal physics, J. Mech. Phys. Solids 5 (3) (1957) 223.
[47] R. Cahn, A new theory of recrystallization nuclei, Proc. Phys. Soc. A 63 (4) (1950) 323–336.
[48] R. Sandström, B. Lehtinen, E. Hedman, I. Groza, S. Karlsson, Subgrain growth in Al and Al-1% Mn during annealing, J. Mater. Sci. 13 (6) (1978) 1229–1242.
[49] S. Varma, B. Willits, Subgrain growth in aluminum during static annealing, Metall. Trans. A 15 (7) (1984) 1502–1503.
[50] W. Blum, C. Schlögl, M. Meier, Subgrain Formation and Subgrain Boundary Migration in Al-5Mg during High Temperature Deformation in the Range of Class A Behaviour in Comparison with Pure Aluminium, Int. J. Mater. Res. 86 (9) (1995) 631–637.
[51] W. Boas, J. Bowles, The effect of crystal arrangement on "secondary recrystallization" in metals, J. Inst. Met. 74 (1947) 501–519.
[52] R. Doherty, J. Szpunar, Kinetics of sub-grain coalescence—A reconsideration of the theory, Acta Metall. 32 (10) (1984) 1789–1798.
[53] L. Murr, Interfacial phenomena in metals and alloys, Phys. Unserer Zeit 8 (1) (1975).
[54] Y. Huang, F. Humphreys, Measurements of grain boundary mobility during recrystallization of a single-phase aluminium alloy, Acta Mater. 47 (7) (1999) 2259–2268.
[55] A. Rollett, M. Alvi, A. Brahme, J. Fridy, H. Weiland, J. Suni, S. Cheong, Texture-dependent recrystallization in aluminum 1050, in: Materials Forum, Vol. 28, 2005, pp. 1173–1178.
[56] X. Chen, W. Wang, H. Yang, G. Huang, D. Xia, A. Tang, B. Jiang, H.N. Han, F. Pan, Microstructure evolution, mechanical properties and deformation characteristics of ultrafine-grained annealed pure aluminum, Mater. Sci. Eng. A 846 (2022) 143320.